Coarsening- and Creep Resistance of Precipitation-Strengthened Al-Mg-Zr Alloys Processed by Selective Laser Melting

S. Griffiths[1], J.R. Croteau[2], M.D. Rossell[3], R. Erni[3], A. De Luca[1], N.Q. Vo[2], D.C. Dunand[4], C. Leinenbach[1]*

1. Empa-Swiss Federal Laboratories for Materials Science and Technology, Laboratory for Advanced Materials Processing, Überlandstrasse 129, 8600 Dübendorf, Switzerland
2. NanoAl LLC, 260 Eliot St, Ashland, MA 01721, USA
3. Empa-Swiss Federal Laboratories for Materials Science and Technology, Electron Microscopy Center, Überlandstrasse 129, 8600 Dübendorf, Switzerland
4. Department of Materials Science and Engineering, Northwestern University, Evanston, IL 60208, USA

*) Corresponding author: christian.leinenbach@empa.ch, Tel: +41 58 765 4518

Abstract

The coarsening behavior of Al_3Zr precipitates during aging was investigated for two Al-Mg-Zr alloys (Al-3.6Mg-1.2Zr and Al-2.9Mg-2.1Zr, wt.%) processed by selective laser melting (SLM). Scanning transmission electron microscopy (STEM) investigations of peak-aged (400˚C, 8 h) samples reveal both continuous (~2 nm in diameter) and discontinuous (~5 nm wide and hundreds of nanometers in length) coherent, secondary $L1_2$-Al_3Zr precipitates. In-situ STEM experiments showed that aging at 400˚C results in the appearance and growth of both grain-boundary Al_3Zr precipitates, and intragranular nanometer-sized spherical Al_3Zr precipitates in Zr-rich dendritic arms. Heating to 500˚C resulted in the disappearance of most Al_3Zr precipitates and oxide particles. This microstructural evolution sheds light on the evolution of the alloy strength at elevated temperature. For short-term yield tests, as-fabricated samples displayed higher yield strengths than peak-aged samples at temperatures above 150˚C (e.g., 87 vs 24 MPa at 260˚C). This is attributed to coarsening of grain-boundary precipitates during aging, decreasing their ability to inhibit grain-boundary sliding (GBS) of the fine equiaxed grains (~1 μm). For longer term creep tests at 260 ˚C, both as-fabricated and peak-aged samples displayed near-identical creep behavior during a long-duration (168 h) creep test; by contrast, during a shorter duration creep test (8 h), as-fabricated samples are more creep-resistant than samples previously aged at 260 ˚C (threshold stresses of ~40 vs. ~14 MPa, respectively). Again, the creep behavior is consistent with coarsening of grain-boundary precipitates, occurring now during long-duration creep tests at 260 ˚C. An exact creep mechanism could not be isolated due to microstructural changes during testing but is believed to be a combination of GBS and dislocation motion.

1 Introduction

Additive manufacturing (AM) of metallic materials has been the focus of intense industrial and academic research efforts due to the many advantages the process can offer over conventional processing techniques, such as (i) more geometric freedom, (ii) minimal custom tooling, and (iii) rapid prototyping [1]. The process, in a simplistic way, can be viewed as a multipass weld; therefore, it suffers from all of the same problems that plague welded structures, such as hot tearing and high residual stresses. Only weldable metal alloys, such as Al-Si alloys, Ti-6Al-4V and 316 stainless steel, are thus well suited for AM processing. Unfortunately, this limitation implies that a sizeable portion of engineering alloys used in conventional processing routes, namely the precipitation strengthened alloys such as CM247LC, Al-Mg-Si based 6000 series alloys, and the Al-Zn-Mg based 7000 series alloys, cannot easily be manufactured via AM without the occurrence of substantial hot cracking [2,3]. A combination of alloy modification and/or process control to mitigate hot cracking susceptibility (reduction of material freezing ranges and reduction of thermal gradients) is thus required for many precipitation-strengthened aluminum alloys.

Initially, most research on AM of aluminum alloys focused on the Al-Si system [4–8] due to the inherent weldability of this alloy family. Parts have been successfully produced by AM using this class of aluminum alloys; however, they suffer from relatively low strength and low ductility compared to the precipitation-strengthened 2000 (Al-Cu), 6000 (Al-Mg-Si), and 7000 (Al-Zn-Mg) series alloys. Unfortunately, the 2000, 6000, and 7000 series exhibit larger freezing ranges compared to the Al-Si alloys, which make them more prone to hot cracking. Hot cracking during AM of 7000 series alloys could successfully be mitigated by modifying the alloys composition and the powder characteristics. Sistiaga et al. [9] fabricated dense, crack-free parts with selective laser melting (SLM) by using an Al7075 powder blended with elemental Si powder (4 wt.%). The authors attributed the improvement to the lower viscosity of the molten alloy; however, adding large amounts of Si is detrimental for ductility. Martin et al. [2] added nanoscale hydrogen-stabilized Zr particles to the surface of 6061 and 7075 Al powders in order to preferentially nucleate equiaxed grains during solidification, due to the primary precipitation of Al_3Zr. Equiaxed grain microstructures, when compared to the typical columnar grain microstructures of AM aluminum parts, can better accommodate the strain induced by the AM process, thus resulting in crack-free parts.

Recent research on AM of aluminum alloys has focused on Sc- and/or Zr-modified Al-Mg based alloys [10–17]. This class of alloy benefits from solid-solution strengthening from Mg as well as precipitation strengthening from coherent $L1_2$ structured $Al_3(Sc,Zr)$ secondary nano-precipitates, formed on aging, that have a high dislocation cutting resistance and resist coarsening up to temperatures above 400°C [18]. Primary $Al_3(Sc,Zr)$ precipitates formed on solidification also serve as grain-refiners which promote fine, equiaxed, Al matrix grains that increase alloy strength, and are thus also beneficial for hot-crack mitigation. Another benefit of AM

processing is related to the extremely high cooling rates, which allow for increased solute solubility of Sc and Zr. Upon aging, this supersaturated solution induces the precipitation of higher volume fractions of the strengthening $L1_2$-Al_3(Sc,Zr) secondary precipitates compared with that of conventional processing. Designing alloys optimized for fast cooling rates is thus the key to taking full advantages of AM processing. One such alloy is the Al-Mg-Sc-Zr alloy Scalmalloy® (Al-4.6Mg-0.49Mn-0.66Sc-0.42Zr (wt%)) which was shown to have good processability via SLM [16]. Spierings et al. [17] obtained dense (>99%), crack-free Scalmalloy® parts with yield strengths up to 300 MPa in the as-fabricated (SLM) condition, and in a separate study [19], reported a yield strength of 470 MPa for SLM processed Scalmalloy® in the aged condition (325˚C / 4 h). In a second example, Jia et al. [10] also developed an Al_3(Sc,Zr)-strengthened alloy, Al-4.52Mn-1.32Mg-0.79Sc-0.74Zr-0.05Si-0.07Fe (wt%), that takes advantage of the high cooling rates of SLM to allow for supersaturation of Mn. The use of Mn for solid solution strengthening, instead of Mg, would minimize the disadvantages associated with Mg such as: (i) Mg suffers from significant in-process (SLM) evaporation [15] and (ii.) precipitation of the β-phase(Mg_2Al_3) can lead to increased grain boundary corrosion susceptibility [20]. A bimodal microstructure of fine equiaxed grains and columnar grains was also observed, and yield strengths of ~440 MPa and ~560 MPa were reported for the as-fabricated and peak-aged condition (300˚C / 5 h), respectively.

A third example of an aluminum alloy developed specifically for the AM process, is Addalloy®, a Sc-free Al-Mg-Zr-based alloy which is strengthened, after aging, by metastable $L1_2$-Al_3Zr nanoprecipitates instead of stable, but much coarser $D0_{23}$-Al_3Zr precipitates. The alloy also precipitates, upon solidification, primary Al_3Zr precipitates with the same metastable $L1_2$-structure, when high enough cooling rates are achieved [21], such as that experienced in AM. These primary $L1_2$-precipitates again act as grain-refiners which result in an alloy with fine, equiaxed grains. The ability to partially or completely replace the very expensive Sc by much less costly elements, such as Zr, to produce $L1_2$ primary and secondary precipitates is already applied in conventionally cast alloys [22–24]. We have demonstrated in previous studies [15,25] that high density (>99%), crack-free Addalloy® parts can be fabricated via SLM; when peak-aged (400˚C / 8 h), high yield strengths and ductility (~345 MPa and ~20% respectively) are achieved [15].

Prior to more widespread industrial implementation of the aforementioned precipitation strengthened aluminum alloys for additive manufacturing, additional microstructure characterization and understanding of mechanical properties are required. Room temperature mechanical property testing has been investigated for SLM-fabricated aluminum alloys but high-temperature properties are few and even non-existent for the AM fabricated Al_3(Sc,Zr) precipitate strengthened alloys. Significant amount of literature is available on conventionally-cast, $L1_2$-strengthened aluminum alloys, with various elements replacing partially or fully Sc: (i) transition metals (Zr [26], Ti [26], V[27,28], Nb [27,29], Ta [27,29], Hf [30], Mo [31]) which also improve nanoprecipitate coarsening resistance, or (ii) lanthanides (Er, Y, Sm, Gd, Tb, Dy, Ho,

Tm, Yb, Lu) which improve creep resistance [32,33] by increasing the lattice mismatch between nanoprecipitates and matrix [18], and (iii) solid-solution strengthener (Mg, Li) [34,35]. Due to the lower lattice mismatch provided by $L1_2$-Al_3Zr nanoprecipitates with the matrix (0.75%), as compared to Al_3Sc (1.32%) [18], the creep resistance of binary Al-Zr alloys is lower than for binary Al-Sc alloys, at a given nanoprecipitate size and volume fraction [36]. The high super-saturation of Zr achievable in the AM process, and thus the high volume fraction of nanopre-cipitates, could however further improve the creep resistance of Sc-free Al-Zr based alloys, despite the low lattice mismatch. The effect of Mg solid solution on creep resistance at 300 °C was investigated in the case of a Al-2Mg-0.2Sc (wt.%) alloy. While the presence of Mg did not affect the estimated creep threshold stress, for a given nanoprecipitate size and volume fraction, the active deformation mechanism appears to change from dislocation climb in Al-0.2Sc (wt%) to dislocation glide in the ternary alloy, as evidenced by the change in stress exponent. Uzan et al. [37] reported on the creep properties of an SLM printed Al-10Si-Mg (wt.%) tested in the 225-300˚C temperature range at stresses in the 117-147 MPa range. They described a disloca-tion creep mechanism and likened the creep resistance of the SLM printed alloy to that of par-ticle reinforced aluminum composites.

The aging response and room-temperature mechanical properties of SLM-produced Ad-dalloy® have been previously reported [15], albeit without a nanometric-level microstructural investigation. When isothermally aged at 400˚C , the alloy exhibits two hardness peaks, the first after 2 h, and the second after 6-8 h of aging, which were hypothesized to correspond to $L1_2$-Al_3Zr precipitation occurring discontinuously (elongated fan-like precipitates) and continu-ously (equiaxed precipitates), respectively [15]; however, no microstructural evidence was pre-sented. After aging to the second peak hardness (400˚C / 8 h), the alloy exhibits a ~354 MPa tensile yield strength with a ~20% tensile elongation [15]. The combination of high yield strengths and high ductility was attributed to the bimodal grain structure of the alloy.

Here, we present a thorough investigation of the nano-scale precipitation with the aim of elucidating the origin of the two hardness peaks reported in Croteau *et al.* [15]. We also inves-tigate the Al_3Zr coarsening behavior of Addalloy® with a combination of in-situ and ex-situ scanning transmission electron microscopy (STEM) experiments. Elevated temperature creep properties are reported (for the first time for a SLM fabricated $L1_2$ precipitate-strengthened Al alloy) and correlated with the concurrent microstructure evolution.

2 Experimental methods

2.1 Materials and additive manufacturing

Addalloy®, an Al-Mg-Zr alloy developed by NanoAl LLC (Ashland, MA, USA) for additive manufacturing, was inert-gas atomized by Nanoval (Berlin, Germany) in two variants, with low and high Zr content: Al-3.60Mg-1.18Zr and Al-2.90Mg-2.10Zr (wt. %, as measured by ICP-OES). For the lower-Zr alloy, two batches were used, with different powder size distributions: Batch 1 (10-45 μm, d_{50}=14 μm) and Batch 2 (25-45 μm, d_{50}=37 μm). For the higher-Zr alloy, a single batch was utilized (Batch 3, 10-45 μm, d_{50}=24 μm). The small batch sizes of the experimental Al-Mg-Zr alloy necessitated the use of numerous batches. Comparisons between results, such as mechanical property results, were only made between samples fabricated from identical batches.

Samples were fabricated using a powder-bed, selective laser melting machine (M2 Concept Laser, Germany) outfitted with a 200 W 1070 nm fiber-laser operating in continuous wave mode with a 90 μm spot size. Argon shielding gas kept oxygen content in the build chamber below 1% during processing. All batches were processed using a chess scanning strategy with full 200 W laser power, 200 mm/s scanning speed, and a 135 μm hatch spacing. Batch 1 and 3 powders were processed with a 30 μm layer thickness and Batch 2 with a 40 μm layer thickness (due to the larger powder size). Cubical samples (8×8×8 and 10×10×10 mm) were fabricated from the three powder batches for microstructural characterization purposes. Cylindrical samples (10 mm diameter, 34.5 mm height, with build direction along the long axis) and bar samples (10 mm wide, 75 mm long, 34.5 mm height, with build direction along the height axis) were fabricated from the high-Zr alloy (Batch 3) for mechanical testing.

2.2 Mechanical testing

The bar samples were machined into dog-bone tensile samples (long axis of dog-bone transverse with the build direction) with threaded grips and a gauge section with 3 mm diameter and 12 mm length. These samples were tested either in their as-fabricated state or after a thermal treatment conducted in air. High-temperature tensile tests were conducted in air using a mechanical test frame operated at a fixed strain rate of $10^{-4}\,\mathrm{s}^{-1}$. Each sample was tested at multiple temperatures by deforming the sample just beyond its yield stress followed by unloading. The first such mechanical cycles was performed at 260˚C, followed by five subsequent load-unload cycles performed at 205, 177, 150, 100 and 20˚C, with a 30 min soaking time after the sample reached each temperature.

For the creep tests, the cylindrical and bar samples were machined into dog-bone tensile samples (with their long axis parallel to the build direction for the cylinders, and transverse for the bars) with threaded grips and a gauge section with 3 mm diameter and 12 mm length. Creep tests were conducted on the dog-bone specimens in air using tensile dead-loading, with the

deformation of the sample measured by a digital displacement gauge in the cold part of the load train. After reaching thermal equilibrium, mass was added incrementally to the dead-load apparatus. Steady-state creep rate was taken as the linear region of the displacement curve. After a steady-state creep rate was reached, additional mass was added. Following this procedure, a full creep curve was generated in approximately one week. A variant of this test was performed in which mass was added at 30 min intervals until the first deformation was observed, at which time we reverted to prior method of observing steady-state creep, so that this test took approximately 8 h to generate a full curve.

2.3   Microstructure characterization

Sample cubes for microstructure characterization were cold-mounted in epoxy, ground, polished with a 3 μm monocrystalline diamond suspension and lapped with 50 nm colloidal silica. Sections parallel to the build direction were characterized with a Scanning Electron Microscope (FEI NanoSEM 230) in backscatter mode. Fractured creep samples were cold-mounted in epoxy (sections parallel to the build direction), ground (halfway through the gauge section), polished with a 3 μm diamond suspension and lapped with 50 nm colloidal silica.

Lamellae for scanning transmission electron microscopy (STEM) analysis were extracted from the aforementioned sample cubes (lamellae is perpendicular to build direction) and fractured creep dog-bone samples (lamellae is perpendicular to build direction and taken from the deformed gauge section) using an FEI Helios NanoLab 600i focused ion beam (FIB). The use of Ga^+ ions in the lamellae preparation resulted in some Ga contamination at the grain boundaries and at precipitate-matrix interfaces. STEM was performed on an FEI Titan Themis microscope operated at 300 kV and equipped with a probe spherical aberration corrector and a SuperEDX system (ChemiSTEM technology) with four silicon drift detectors for energy-dispersive X-ray (EDX) spectroscopy. A convergence semi-angle of 25 mrad was used in combination with an annular dark field (ADF) detector with inner and outer collection semi-angles of 53 and 200 mrad, respectively. STEM-EDX spectrum images (background corrected) were pre-filtered and displayed as quantified wt.% maps.

Two *in situ* STEM thermal aging experiments were performed with a Protochips Fusion 500 heating stage on the same FEI Titan Themis microscope described above. A first sample was extracted from the coarse-grain region of a sectioned Al-3.60Mg-1.18Zr (wt.%) cube (Batch 1) and a second sample was extracted from a fine-grain region of the same cube. Both extractions were done with an FEI Helios NanoLab 600i focused ion beam (FIB) so that the lamellae were perpendicular to the build direction. The *in situ* aging experiment of the coarse-grain sample began with a 160 s ramp from 20 to 400°C. The sample was held for 480 s before it was quenched back to 20 °C. EDX mapping was conducted on regions of interest on the quenched sample. The sample was subsequently held at 400°C for 600 s. Finally, the sample was heated to 500°C and held at that temperature for 116 s until the diffusion of Pt from the protective layer of the lamella destroyed the sample. The fine-grain sample was exposed to a

range of temperatures, from 150 to 350˚C (with 25˚C increments) over 64 min. Once the sample reached 350˚C, it was held there for 48 min to observe the precipitate growth. The sample was then heated from 350 to 600˚C (with 25˚C increments) over 40 min until its destruction at 600˚C.

3   Results

3.1   Microstructure of As-fabricated Samples

Both as-fabricated and aged samples display a duplex grain microstructure consisting of fine-grain regions at the bottom and sides of the melt pool, and coarser-grained regions in the remainder of the melt pool (Figure 1(a)). No significant difference in grain microstructure was observed between samples fabricated from the high- and the low-Zr containing powders. As shown in previous studies [15,25], the fine-grain regions consist of sub-micron (~0.8 μm) equiaxed grains with a random crystallographic orientation, and the coarse-grain regions comprise columnar grains (~1x10 μm), with a slight (100) texture. The fine-grain region displays sub-micron (~100 to 200 nm) $L1_2$-structured Al_3Zr primary precipitates, which are coherent with the matrix and have a similar number density as the α-Al grains (Figure 1b), consistent with these primary precipitates nucleating α-Al grains [15,25]. The coarse-grain regions do not display these primary $L1_2$-Al_3Zr precipitates but contain Zr in solid solution [15,25]. Similar microstructures have been observed by Spierings *et al.* for as-SLM-fabricated Al-Mg-Sc-Zr-Mn alloys containing primary $L1_2$-$Al_3(Zr,Sc)$ precipitates.
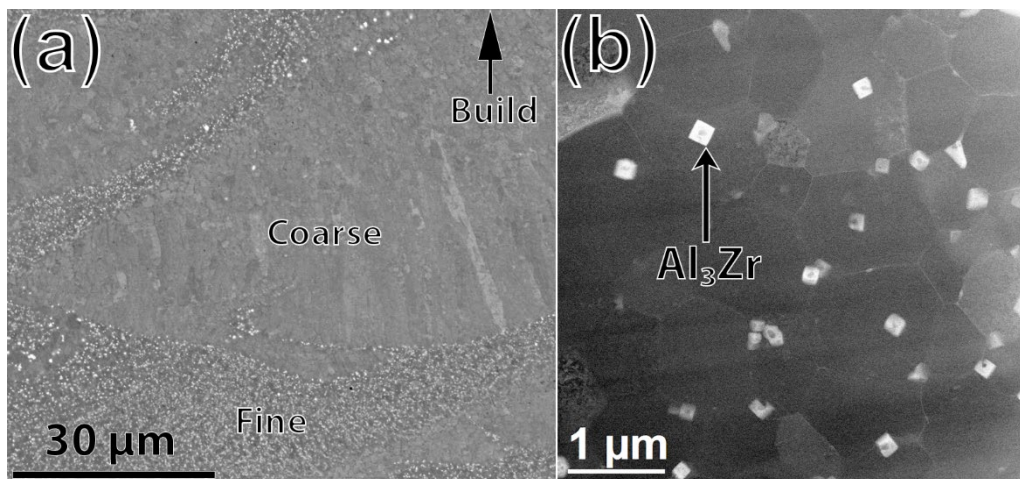

Figure 1: (a) BSE image of an as-fabricated sample (Al-2.90Mg-2.10Zr, wt. %, Batch 3) with 30 μm layer thickness, showing bands of fine-grain regions containing primary Al_3Zr precipitates (white dots) and coarse-grain regions free of Al_3Zr precipitates. (b) ADF STEM image of a precipitate-rich region in Al-3.60Mg-1.18Zr (wt.%, Batch 2) showing cuboidal, submicron $L1_2$-Al_3Zr precipitates and micron-sized α-Al grains.

Figure 2 shows an ADF-STEM image and a series of STEM EDX maps taken from a coarse-grain region of the Al-3.60Mg-1.18Zr, wt.% as-fabricated sample. As expected, no primary $L1_2$-Al_3Zr is present, and Zr is detected uniformly throughout the mapped region, indicative of solid-solution. Magnesium enrichment and Al depletion are observed at the grain boundaries, but there is no evidence of a continuous secondary phase (i.e., β-Al_2Mg). Three types of precipitates are visible: (i) Mg- and O-rich particles, ~100 nm in diameter, which are likely oxide inclusions originating from the powder surface and/or created during the printing process;

(ii) Mg- and Si-rich precipitates, ~50 nm in diameter, which are located both within the grains and at grain boundaries; (iii) Fe-rich precipitates, ~50 nm diameter, on the grain boundaries. The occurrence of Fe-rich and Si-rich precipitates is discussed below.
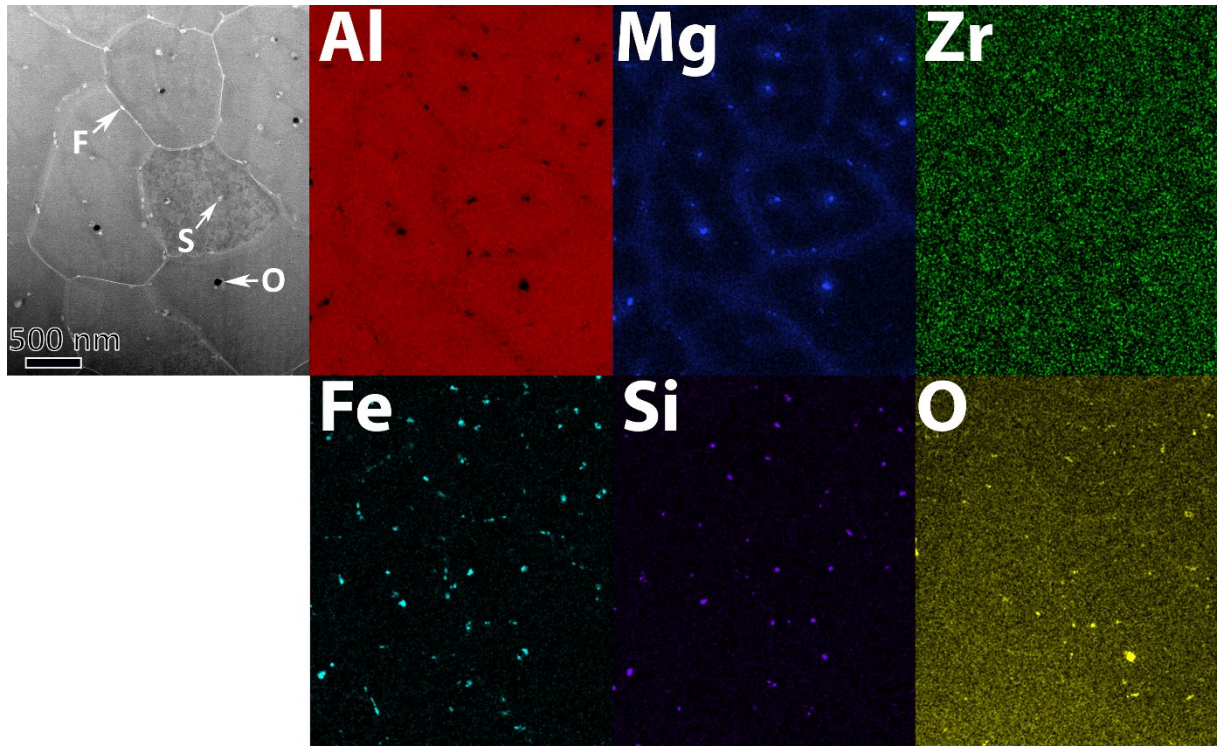

Figure 2: Coarse-grain region of an as-fabricated sample (Al-3.60Mg-1.18Zr, wt.%, Batch 1) imaged via STEM (ADF- image and elemental EDX maps using Si-K, Zr-K, Al-K, Mg-K, Fe-K and O-K lines) showing three types of precipitates : (i) Mg- and O-rich oxide particles, ~100 nm in diameter; (ii) Mg- and Si-rich particles, ~50 nm in diameter, (iii) Fe-rich particles, ~50 nm diameter, on the grain boundaries. One example for each type of precipitates is highlighted on the ADF-STEM image, with labels O, S and F, respectively.

3.2 Aging Response

Figure 3 displays an ADF-STEM image and the corresponding STEM-EDX maps taken from the coarse-grain region (grains appear sub-micron as the TEM lamellae was sampled perpendicular to the grains long dimension) of a sample aged at 400 ˚C for 8 h (second peak aging). In addition to the Zr-enriched precipitates, the same three types of precipitates as in the as-fabricated state (Fig. 2) are present. First, Zr-rich precipitates are observed at the grain boundaries (larger, equiaxed in shape), expected to be primary $L1_2$-Al_3Zr formed during solidification; finer $L1_2$-Al_3Zr nanoprecipitates within the grains, filamentary in shape, have also appeared due to aging. Second, the same Mg- and O-rich equiaxed oxide particles formed during printing (~100 nm in diameter) are still present, and mostly at grain boundaries. Finally, the same Fe-rich particles are also observed, albeit at a lower number density and larger size when compared to as-fabricated state (Fig. 3 shows a ~100 nm precipitate, twice the original size in Fig. 2).
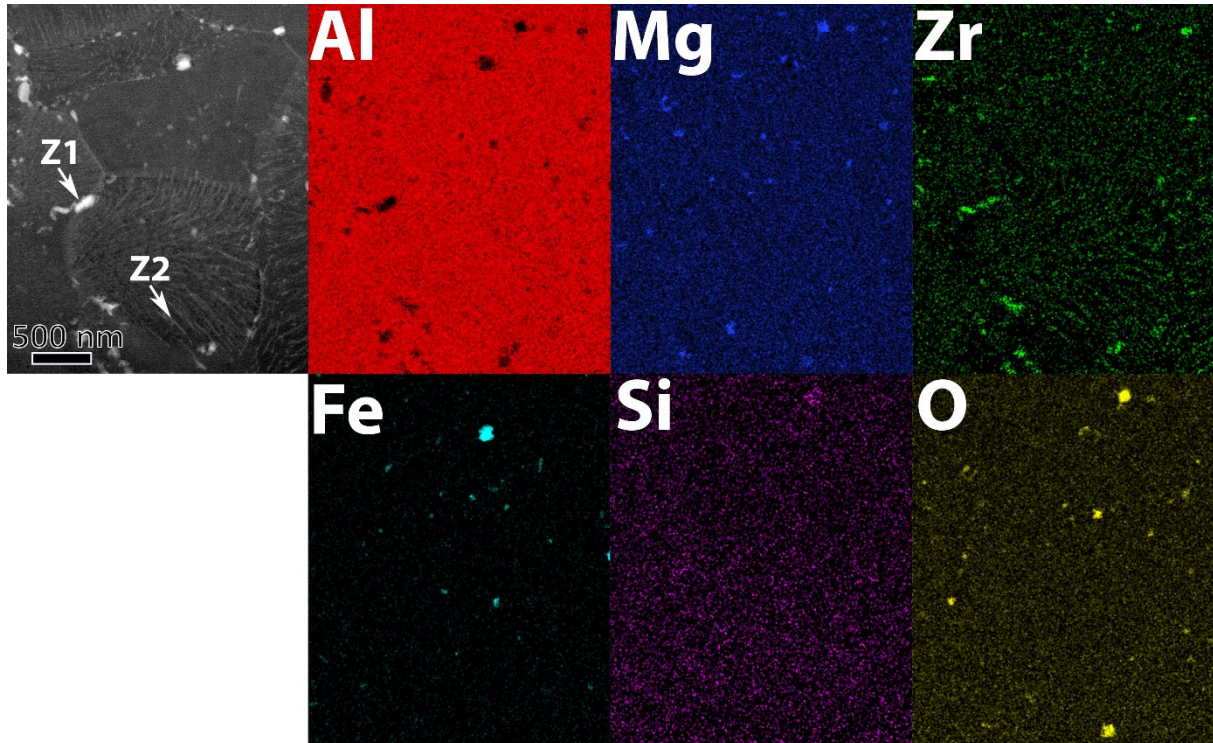
Figure 3: Coarse-grain region of a peak-aged sample (400˚C for 8 h, Batch 1) imaged via STEM (ADF- image and elemental EDX maps using Si-K, Zr-K, Al-K, Mg-K, Fe-K and O-K lines) showing three types of precipitates : (i) Al_3Zr precipitates consisting of larger, equiaxed precipitates (labelled Z1) and finer, elongated precipitates within grains (labelled Z2); (ii) Mg- and O-rich oxide particles (O) located at grain boundaries; (iii) Fe-rich precipitates (F) located grain boundary.

Closer examination of the peak-aged sample shown in Figure 3 illustrates the two types of Zr-rich precipitates (spherical and acicular) within the grains (Figure 4(a)). Although both types of precipitation are observed in the fine-grain region as well, to a lesser extent, the following figures and discussion focus on the observations made in the coarse-grain region. High-resolution ADF-STEM of the upper half of the highlighted region of Figure 4(a) reveals spherical precipitates ~2 nm in diameter (Figure 4(b)). A fast Fourier transform (FFT) of Figure 4(b), which for our purpose can be treated as a selected area diffraction pattern (SAD), reveals the 010-type superlattice reflections of the $L1_2$ structure (Figure 4(c)), consistent with metastable $L1_2$-Al_3Zr precipitates which forms upon aging of super-saturated solid solution. A high-resolution ADF-STEM image of the bottom half of the highlighted region in Figure 4(a) shows the presence of narrow (~5 nm wide), highly elongated (hundreds of nm) filamentary precipitates (Figure 4(d)). An FFT of Figure 4(d) reveals again the 010-type superlattice reflections of the $L1_2$ structure (Figure 4(e)). STEM-EDX mapping of the boxed region in Figure 4(a), shown in Figure 5, indicates that these filamentary precipitates are enriched in Zr, indicating that they are also the $L1_2$-structured Al_3Zr phase.
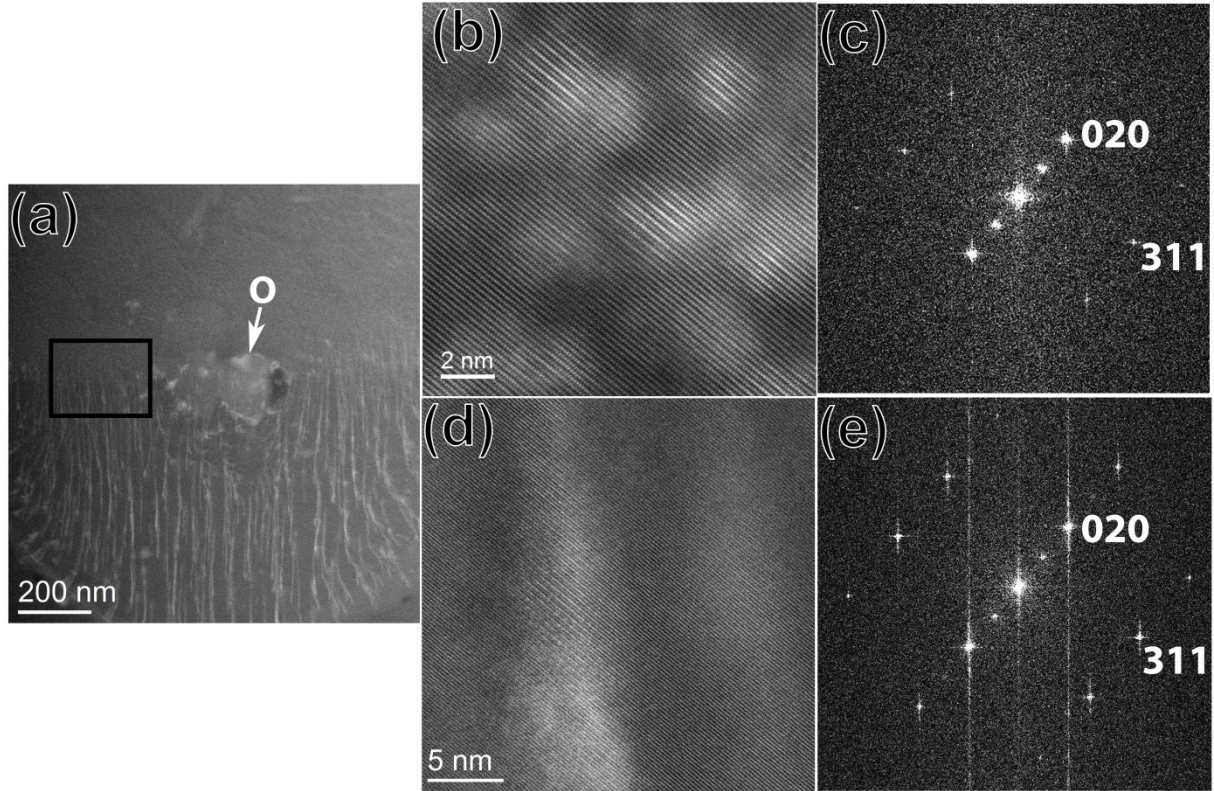
Figure 4: (a) STEM ADF-image of a coarse-grain region of a peak-aged (400°C / 8 h) sample (Al-3.60Mg-1.18Zr, wt.% Batch 1) showing: (i) nanometric equiaxed Al$_3$Zr precipitates formed via continuous precipitation (upper grain) and (ii) elongated, aligned Al$_3$Zr precipitates formed via discontinuous precipitation. An oxide particle (O) is present at the image center (b) High-resolution ADF-STEM image of equiaxed Al$_3$Zr nano-precipitates (2 nm in diameter, continuous precipitation) in the upper half of boxed region in (a). (d) High-resolution ADF-STEM image of the 5 nm-wide, highly-elongated Al$_3$Zr precipitates formed by discontinuous precipitation in the lower half of boxed region in (a). (c, e) FFT of images (b) and (d), respectively, show the 010-type superlattice reflection of the metastable L1$_2$ structure for Al$_3$Zr.
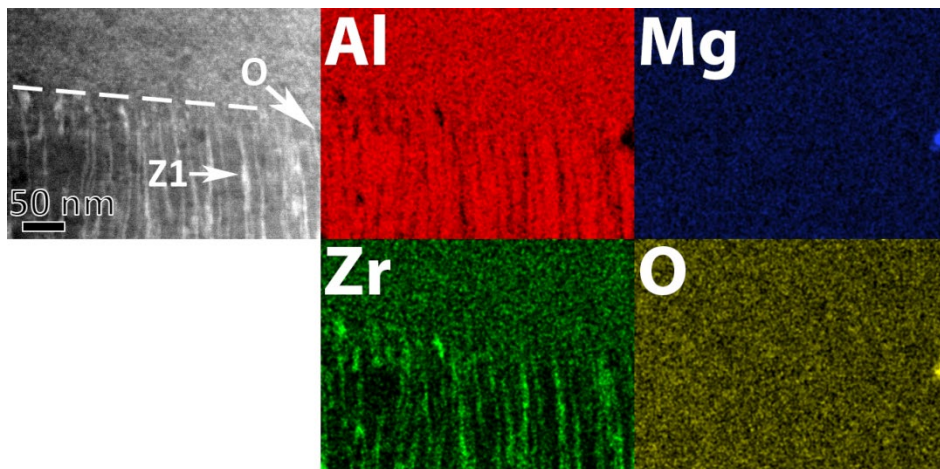

Figure 5: STEM ADF-image and elemental EDX maps of the region highlighted by the black box in Figure 4, showing elongated, discontinuous L1$_2$-Al$_3$Zr precipitates (labelled Z1) and one Mg- and O-rich oxide particle (O) at the interface between continuous and discontinuous precipitation (dashed line). Chemical analysis was performed using the Zr-K, Al-K, Mg-K, and O-K lines.

3.3 In-Situ Aging Response

Two in-situ STEM aging experiments were carried out to investigate the evolution of primary and secondary precipitates during thermal exposure. The use of in-situ STEM experiments, as opposed to ex-situ, allows for the direct monitoring of individual features of interest. The first experiment was performed with a lamella taken from a coarse-grain region, with no primary Al_3Zr phase, in an as-fabricated Al-3.60Mg-1.18Zr (wt.%, Batch 2) sample. An ADF-STEM image of the lamella prior to thermal exposure is shown in Figure 6(a). Several spherical, Mg- and O-rich particles, ~100 nm in diameter and assumed to be oxides, are observed both on grain boundaries and within the grains (a few are identified by black arrows in Fig. 6(a)). The sample was ramped from room temperature to 400˚C in 160 s and then held at this temperature for 480 s. An ADF-STEM image taken thereafter is shown in Figure 6(b). Numerous white precipitates, assumed to be $L1_2$-Al_3Zr, are observed to nucleate both on the grain boundaries (~100 nm diameter, highlighted by white arrows, nucleation began during the ramp at 360˚C) and within the grains (nanometer scale, observed starting at the end of the ramp to 400˚C). The $L1_2$-Al_3Zr nanoprecipitates within the grain are grouped in dendritic regions, as evidenced in the inset of Figure 6(b)), consistent with the peritectic solidification of dilute Al-Zr alloy causing Zr segregation in Zr-rich dendritic arms and Zr-poor interdendritic regions [38].

Figure 6(e) shows a STEM-EDX map taken after quenching the sample back to room temperature after 480 s at 400˚C. The ring-like features highlighted by the black arrows in Figure 6(a) are Mg- and O- rich oxides particles. Particles similar to the small dark precipitates highlighted in Figure 6(c) are enriched in Mg, F, and O. Although the source of the F is unknown, the particles are assumed to be oxides. The bright nanoparticles observed during the aging treatment are enriched in Zr. Crystallographic data was not obtained during this specific experiment, but given the crystallographic data obtained from the peak aged sample shown in Figure 4, they are assumed to be the metastable, $L1_2$-structured Al_3Zr.

Figure 6(c) presents a subsequent ADF-STEM image taken after an additional 600 s of exposure at 400˚C. Compared to Figure 6(b), there is a decrease in the number of grain-boundary Al_3Zr precipitates (in particular on the right grain boundary) which is associated with a growth of the Al_3Zr precipitate located in the lower right quadrant (black arrow). Also, a new acicular precipitate grew in the bottom left (white arrow), which may be the Al_3Zr with the stable $D0_{23}$ structure, identified based on its acicular geometry (but this was not confirmed via crystallographic analysis). Furthermore, an increase in the number of small (~10-20 nm in diameter) dark precipitates (highlighted by empty arrow) was observed. The increase in number of oxide particles during the experiment may be the result of the coarsening of existing oxide particles that make them more visible. Further aging at 500˚C was performed on the sample (Figure 6d); only the disappearance of the intragranular Al_3Zr particles and growth of the acicular Al_3Zr precipitate were observed.
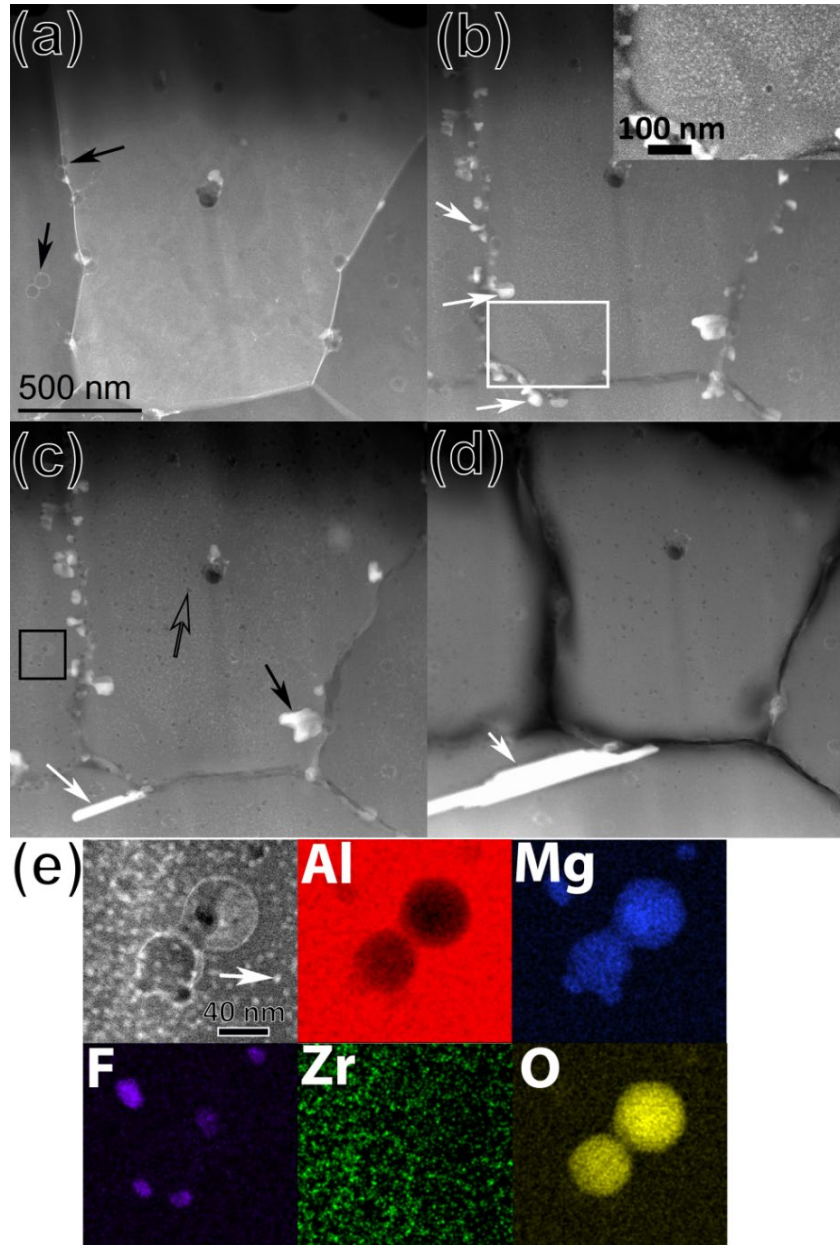
Figure 6: In-situ experiment of coarse-grain region of as-fabricated Al-3.60Mg-1.18Zr (wt.%), Batch 2.
(a) ADF-STEM image of the region of interest prior to thermal exposure. Oxides are highlighted by
black arrows. (b) ADF-STEM image after 420 s of exposure at 400°C showing Al_3Zr precipitates (white
arrows) and nano-scale Al_3Zr precipitates within the grains, highlighted by the white box and enlarged
in the inset. (c) ADF-STEM image after 1000 s of exposure at 400 °C. Coarsening of equiaxed $L1_2$-
Al_3Zr precipitates at grain-boundary occurred (black arrow). An acicular precipitate expected to be $D0_{23}$-
Al_3Zr is observed (white arrow). (d) ADF-STEM image after 30 s at 500°C showing further growth of
the acicular $D0_{23}$-Al_3Zr precipitate (white arrow) (e) Higher magnification ADF-STEM image and
STEM EDX map of the region highlighted by the black box in (c). Two spherical Mg- and O-rich oxide
particles are surrounded by much finer Al_3Zr nanoprecipitates (white arrow). Particles enriched with F
and Mg are also observed, but of unknown origin. Chemical analysis was performed using the Zr-K, Al-
K, Mg-K, F-K and O-K lines.

Figure 7 presents a second in-situ STEM experiment performed on a lamella taken from a fine-grained region of as-fabricated Al-3.60Mg-1.18Zr (wt.%, Batch 2). An ADF-STEM image of the room temperature condition is shown in Figure 7(a). Numerous primary $L1_2$-Al_3Zr precipitates are observed within the central grain. During the 64 min ramp to 350°C, a grain boundary precipitate (unidentified) is observed to form at 200°C and later disappears at 300°C (not shown). Precipitate coarsening at the grain boundaries is assumed to occur faster due to short circuit diffusion on the boundaries. Figure 7(b) shows the ADF-STEM image taken after a 64 min ramp to 350°C. Two horn-like features are observed growing from the corners of one of the Al_3Zr precipitates. The grain boundary also appears to shift from its initial position, before being pinned after the appearance of a dark particle (black arrow). The horn-like feature was observed to grow during the course of the 48 min of exposure at 350°C (Figure 7(c)). A further movement of the grain boundary is observed to follow the horns. A high-resolution ADF-STEM image of the rightmost horn is shown in Figure 7(e). The horn is epitaxially grown from the Al_3Zr precipitate, with the corresponding FFT, shown in Figure 7(f), confirming the existence of 010- and 100- type superlattice reflections consistent with an $L1_2$ structure. The sample was subsequently heated to 500°C, Figure 7(d). The horn-like features disappeared and the particle corners became rounded. Further heating to 600°C induced additional coarsening (not shown).
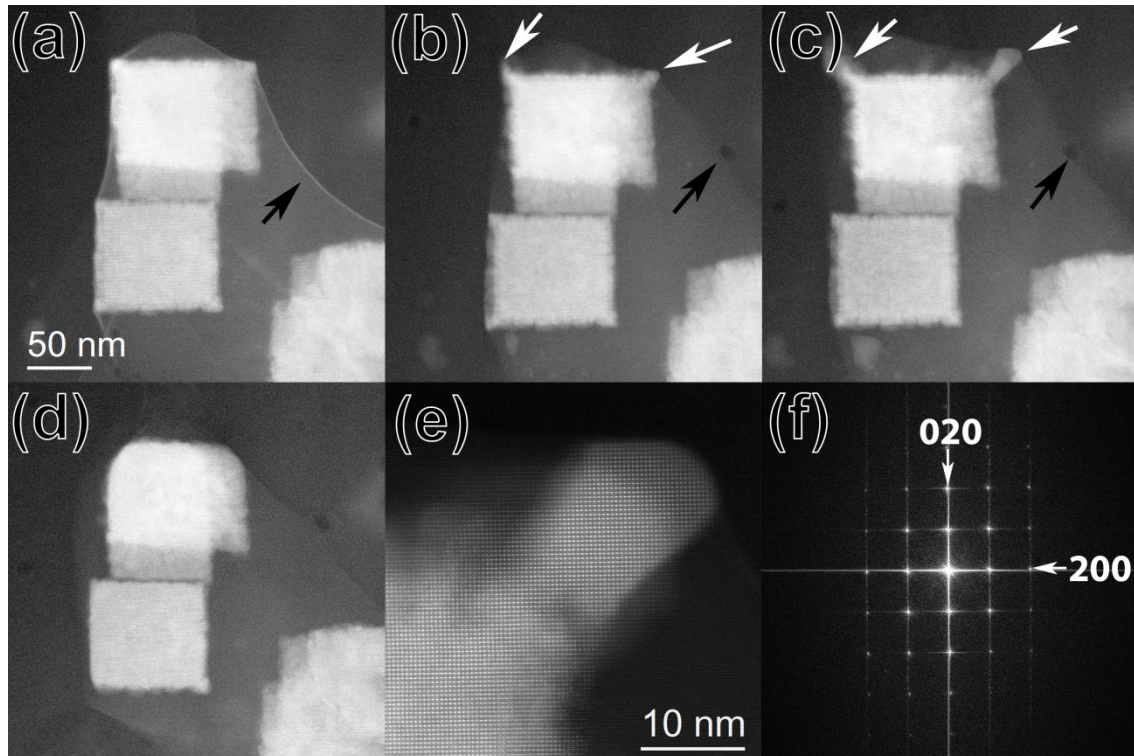

Figure 7: In-situ STEM heating experiment of a fine-grain region of as-fabricated Al-3.60Mg-1.18Zr (wt.%, Batch 2): (a) ADF-STEM image of the region of interest prior to thermal exposure (b) ADF-STEM image taken after a 64-min ramp to 350°C. Horns have grown on the nanoprecipitate corners (white arrow) and grain-boundary movement has occurred (black arrow) (c) ADF-STEM image taken after a subsequent 48 min-exposure at 350°C. Further growth of the horn features occurred. (d) ADF-

STEM image taken after temperature was increased to 500˚C during a 28-min ramp. The horns previously observed at 350˚C disappeared at 450˚C, during the ramp to 500˚C. (e) High-resolution ADF-STEM image of a horn feature, from precipitate imaged in (c), showing epitaxial growth of a horn feature. (f) Diffraction pattern created by FFT of images (e) and (d), respectively) showing the 100- and 010-type superlattice reflections of the metastable $L1_2$ structure for Al_3Zr.

3.4 High-Temperature Mechanical Properties

3.4.1 Tensile Properties

The temperature-dependence of the yield strength is shown in Figure 8 for Al-2.90Mg-2.10Zr (wt.%, Batch 3), in the as-fabricated, peak-aged, and overaged states. Each data point is the value of one transverse samples (additional mechanical property tests on as-fabricated and peak-aged samples are shown in Supplement Figure 3). The peak-aged samples (400°C / 8h) exhibit the highest room-temperature yield strength (330 MPa) but lower strengths as compared to the as-fabricated sample at temperatures at and above 150°C, dropping to 24 MPa at 260˚C. The alloy in the overaged state (aged at 400˚C for 60 h, corresponding to a 10% drop from peak-hardness [15]) shows a lower room-temperature strength (300 MPa) as compared to the peak-age state; this difference is maintained up to 150 ˚C (173 MPa), but disappears above that temperature. Interestingly, the as-fabricated samples, which have a lower room-temperature strength (295 MPa) than the aged samples, have far superior strength at elevated temperatures (87 MPa at 260˚C).
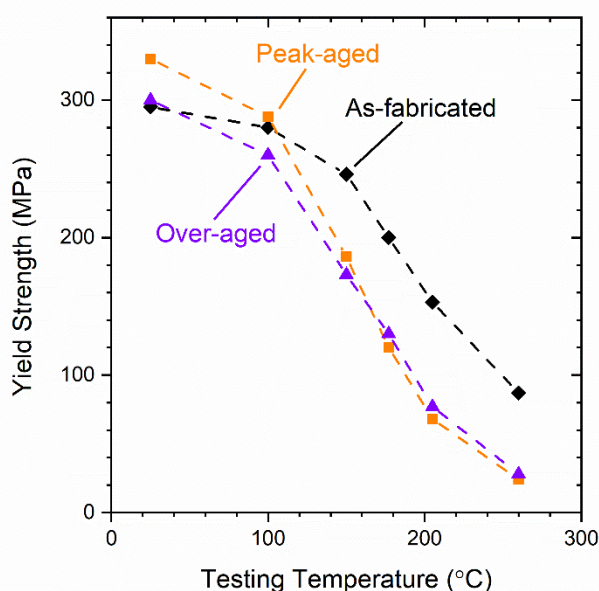

Figure 8: Temperature dependence of yield strength for the high-Zr alloy, Al-2.90Mg-2.10Zr (wt. %, Batch 3), in three conditions: as-fabricated, peak-aged (400ºC, 8 h), and over-aged (400ºC, 60 h). Tests were performed on single samples (transverse orientation), from the highest to the lowest temperature.

3.4.2 Creep Properties

Results of creep testing at 260°C (total creep duration $t_c = 168$ h and $t_c = 8$ h) of as-fabricated, peak-aged, and under-aged high Zr-alloy (Al-2.90Mg-2.10Zr, wt.%, Batch 3) samples are shown in Figure 9, in double-logarithmic plots of secondary strain rate vs. stress (A displacement vs. time plot for the as-fabricated sample crept for 168 h is shown in Supplement Figure 4). For the long duration creep tests (168 h), tensile loading started at ~5 MPa and was incrementally increased; no deformation was measured within the first 120 h, until a stress of 15 MPa was reached for the peak-aged condition. The short duration tests (8 h) were started with a ~25 MPa load, which was incrementally increased every 30 min so that the full test was concluded within 8 h. In Fig. 9, the 25 MPa point is not marked, since no strain was observed within the 30 min duration of this first step. For the two lowest stress/strain rate data points (as-fabricated, $t_c = 8$ h) plotted on Fig. 9 - for 48 and 58 MPa - steady-state deformation may not have been achieved. The strain rates plotted in Fig. 10 might thus be overestimated.

The very high stress sensitivity of strain rate in Figure 9 is indicative of a threshold stress, likely due to the presence of precipitates. In order to estimate the threshold stress, we used a modified version of the Mukherjee-Bird-Dorn power-law equation for the minimum strain rate $\dot{\varepsilon}$:

$$\dot{\varepsilon} = A\left(\sigma - \sigma_{th}\right)^n \exp\left(\frac{-Q}{k_B T}\right) \tag{1}$$

where A is a constant, σ is the applied stress, σ_{th} is the threshold stress, n is the matrix stress exponent (n indicates the creep mechanism), Q is the matrix creep activation energy, k_B is the Boltzmann constant, and T is the absolute temperature. A best-fit procedure was employed to estimate the threshold stress, using stress exponents of $n = 1$ (diffusional creep), n = 2 (GBS) and $n = 3$ (viscous glide), which correspond to the rate-controlling mechanisms most likely for this alloy. It is apparent from Figure 9 that $n = 2$ and 3 both give satisfactory fit over many orders of magnitudes in strain rates.

The threshold stress for the peak-aged condition (aged 400°C for 8 h) crept for a long duration (168 h) was determined to be 13.4 MPa from fitting the data with a stress exponent of $n = 3$, and 13.7 MPa for $n = 2$. The as-fabricated condition crept for a long duration (168 h) displayed a threshold stress of 14.0 MPa ($n = 3$) and 14.8 MPa ($n = 2$). The as-fabricated samples crept at high loads for short durations (8 h) displayed significantly higher threshold stresses, 39.3 and 41.5 MPa in the parallel and transverse direction, respectively ($n = 3$), and 44.4 and 45.6 MPa in the parallel and transverse direction, respectively ($n = 2$). Again, no significant difference exists in the creep resistance of samples loaded parallel or transverse to the build direction, consistent with isotropic mechanical properties. Finally, the under-aged sample (aged at 260 °C for 168 h), shows a low threshold stress of 15 MPa ($n = 3$) and 20 MPa ($n = 2$), however this test started with a stress of ~25 MPa with a steady-state strain rate already above 10^{-5} s^{-1}, so the accuracy of the threshold stress is lower than for the other tests.
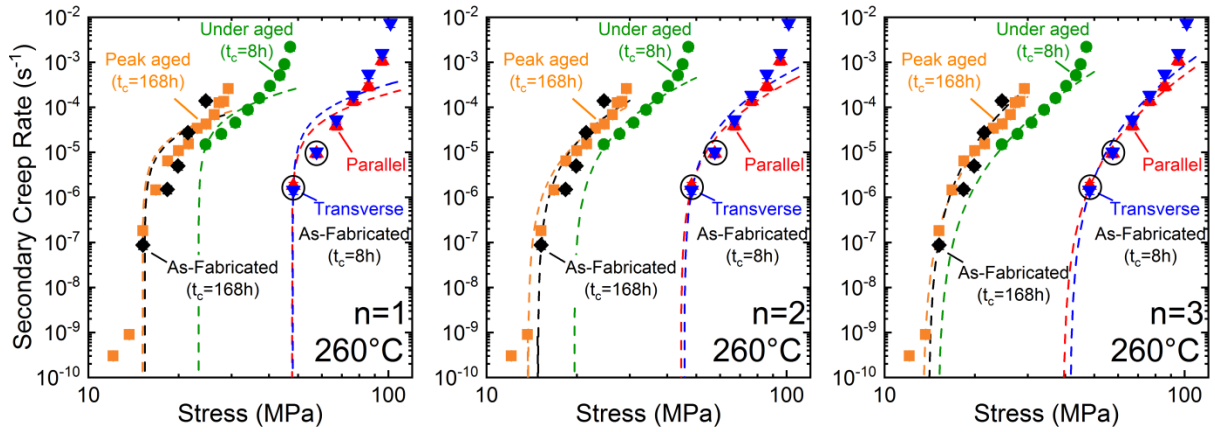
Figure 9: Double logarithmic plot of secondary creep rate vs. stress for creep testing at 260˚C of high-Zr alloy, Al-2.90Mg-2.10Zr (wt.%, Batch 3) in three conditions: as-fabricated, under-aged (260˚C, 168 h), peak-aged (400˚C, 8 h); total creep time is given in parentheses. Data for the as-fabricated state, with a short total creep time of 8 h, were collected by increasing the stress every 30 min, so that steady-state strain rate may not have been achieved at the two lowest strain rates (which are marked with black circles).

3.4.3   Creep Microstructure

Two as-fabricated samples, fractured after creep at 260˚C for 8 and 160 h respectively, were chosen for further microstructural investigation, as they represent two extreme states in the creep data. Fractography (shown in Supplement Figure 5) of the fracture faces of both samples revealed the presence of dimple features indicative of micro-void coalescence during ductile fracture. In a minority of the fracture surface, regions of intergranular fracture were also observed. No significant differences were observed between the two fracture faces.

Figure 10 displays ADF-STEM images and corresponding STEM-EDX maps from the coarse-grain regions of the fractured, as-fabricated samples crept for 8 h (Figure 10a) and 168 h (Figure 10b). The first specimen (as-fabricated and crept for 8 h) exhibits four types of precipitates: (i) Mg- and O-rich particles, ~50-100 nm in diameter, which are located both within the grains and at grain boundaries (ii) Mg- and Si-rich precipitates, ~50-100 nm in diameter, which are located both within the grains and at grain boundaries; (iii) Fe-rich precipitates, ~20-80 nm diameter, on the grain boundaries, (iv) discontinuous Al_3Zr precipitation (shown more clearly in Supplement Figure 6). The other specimen (as-fabricated and crept for 168 h) displays the same precipitates mentioned above, but with larger sizes and lower number density, except for the discontinuous Al_3Zr precipitates: the Mg- and O-rich particles are ~50-100 nm in diameter, the Mg- and Si-rich precipitates at grain boundaries are ~70-180 nm in diameter, and the grain-boundary Fe-rich precipitates are ~50-100 nm diameter.
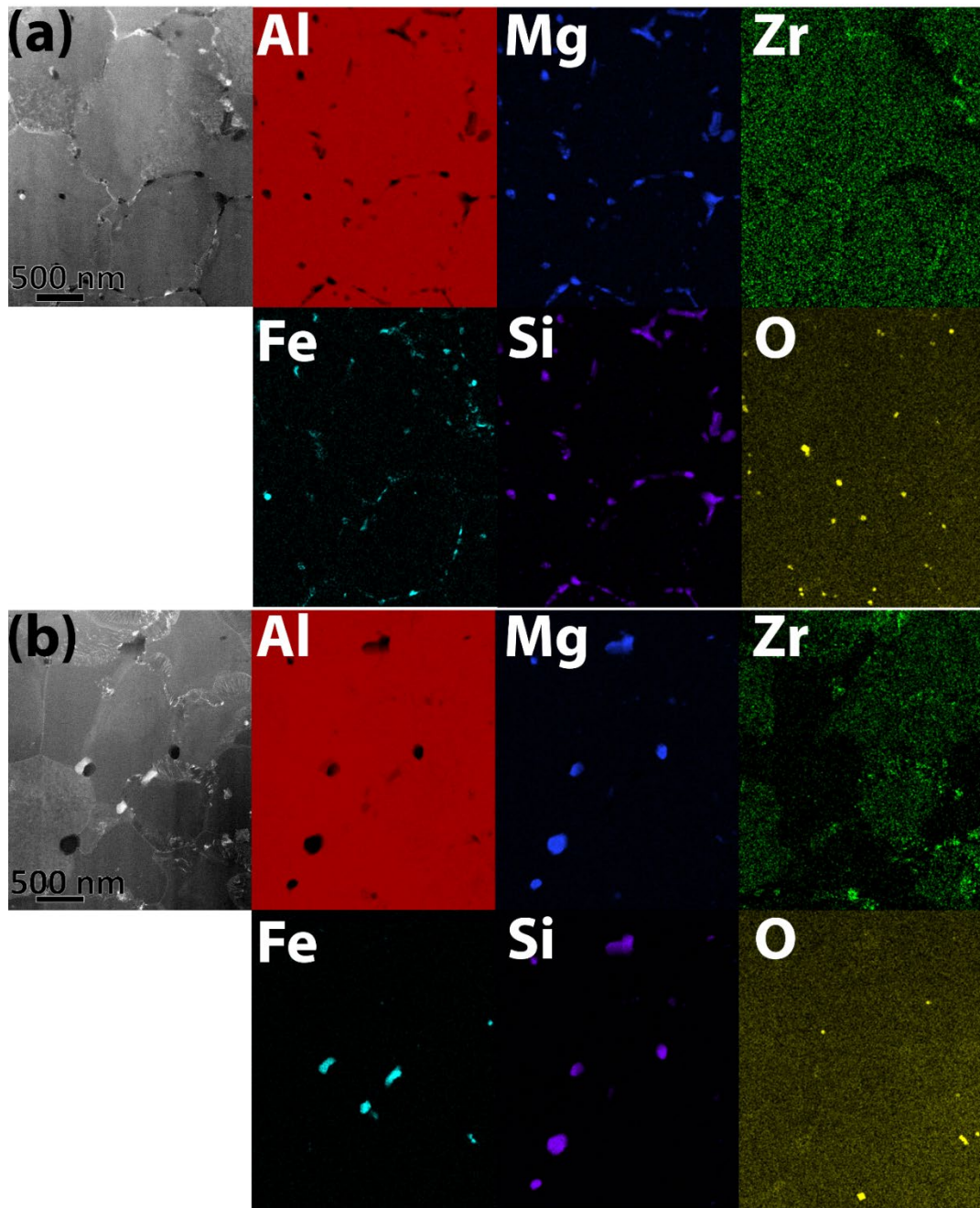
Figure 10: a.) ADF-STEM image and elemental STEM-EDX maps of the coarse-grain region (transverse microstructure) of an as-fabricated sample (Al-2.90Mg-2.10Zr, wt. %, Batch 3, vertical direction) crept-tested to fracture at 260˚C for 8 h. b.) ADF-STEM image and elemental STEM-EDX maps of the coarse-grain region (transverse microstructure) of an as-fabricated sample (Al-2.90Mg-2.10Zr, wt. %, Batch 3, vertical direction) crept-tested to fracture at 260˚C for 168 h. The Fe-rich and Mg+Si-rich precipitates are significantly larger and fewer in the long-duration creep sample when compared to the short-duration creep sample.

4. Discussion

4.1 Microstructure Evolution

We proposed in a prior study [25] that the mechanism behind the observed (Figure 1) bimodal grain microstructure revolves around the peritectic nature of the Al-Zr phase diagram and the changing solidification conditions present in a laser-formed melt pool. At the bottom of the melt pool, the solidification front velocity is low enough that primary Al_3Zr precipitates nucleate and grow in the melt, before inoculating α-Al grains, resulting in a fine, equiaxed, untextured grain structure. As the solidification front velocity increases towards the top of the melt pool, Zr becomes trapped in solid solution and, without Al_3Zr inoculation, columnar grain growth dominates.

After peak aging, grain boundary Al_3Zr particles, fine Al_3Zr nanoprecipitates within the grains, and line-like Al_3Zr precipitates within the grains are observed (Figure 3). Mikhay-lovskaya et al. [39] observed line-like Al_3Zr precipitates, similar to those in Figure 4, after annealing a cast Al-3Mg-0.25Zr (wt.%) alloy for 8 h at 360˚C . Similar filamentary morphology has been observed in many other Al-Zr alloys and is commonly referred to as discontinuous precipitation [39–41]. Phases which are continuously-precipitated within a supersaturated crystalline matrix tend to be uniformly distributed throughout the matrix, and typically have equiaxed, plate- or rod-like shapes showing crystallographic relationships with the matrix; the spherical, coherent Al_3Zr precipitates shown in the upper half of Figure 4(a) are a good example of such continuous precipitates. By contrast, discontinuous precipitation is a form of grain-boundary precipitation that results in colonies of thin lamellar or filamentary precipitates, extending from grain boundaries into the grains, often with a much higher aspect ratio than continuously precipitated rods or plates. Nes and Billdal studied Al_3Zr precipitation in Al-0.8Zr (wt.%) alloys and proposed that grain-boundary movement into a saturated matrix was responsible for the lamellar discontinuous precipitation [40]. In this mechanism, Al_3Zr precipitation initiates at the grain boundary. Since grain boundary diffusion is faster than bulk diffusion, Zr diffuses to the existing precipitates *via* the grain boundaries. As the precipitates grow, they drag the grain boundary into the supersaturated matrix resulting in lamellar growth and a bowed grain boundary. The driving force for this acicular growth results from surface energy minimization between the Al_3Zr precipitates, the supersaturated matrix, and the depleted matrix. The surface energy between the Al_3Zr and the supersaturated matrix is the highest, hence the system minimizes this surface.[40]

As seen in Figure 2, there are numerous precipitates other than Al_3Zr present in the as-fabricated condition. Mg- and O-rich particles are observed and are likely oxides from either the powder surface or in-process oxidation. Also, Mg- and Si-rich particles are located both within the grains and on grain boundaries. Finally, Fe-rich particles are dispersed along the grain boundaries. Silicon and iron are common impurities present in aluminum alloys: Fe has very low solubility in Al and thus precipitates as Fe-rich intermetallic phase, while Si has a

higher solubility in Al, but, in the presence of Mg, it precipitates as the Mg_2Si phase [42]. While the aforementioned elements are impurities and their concentration is kept low, they still play a significant role in mechanical properties as they likely lead to grain boundary pinning. After thermal aging, it was observed that these impurity grain-boundary precipitates coarsen, which effectively reduce their ability to pin grain boundaries. The Fe-rich grain-boundary particles show a significant reduction in number density and increase in size in the peak-aged condition as compared to the as-fabricated condition.

Both grain-boundary Al_3Zr and continuous Al_3Zr precipitation, but not discontinuous Al_3Zr precipitation, were observed during the in-situ STEM experiment of the coarse grain region (Figure 6). The lack of discontinuous Al_3Zr precipitation observed in situ may be due to the limited number of grains examined during the experiment (not all grains have discontinuous precipitation). Also, the contribution of surface diffusion of the thin lamella sample may alter the precipitation behavior by increasing the kinetics of the continuous Al_3Zr precipitation. Furthermore, the finite volume associated with a thin lamella will result in less Zr being available for precipitation. Grain-boundary Al_3Zr precipitates were observed to coarsen during the 400°C exposure and once a temperature of 500°C was reached, only one Al_3Zr particle remained in view (Figure 6(d)). Grain-boundary particle coarsening during thermal exposure will reduce the boundary pinning which, as described later, will have implications on the mechanical properties. The oxide inclusions remained stable even at temperatures of 500°C, which suggest they play a critical role at impeding grain growth during 400°C aging [15].

Primary Al_3Zr precipitate stability and coarsening behavior was studied in the second in-situ STEM experiment (Figure 7). Horn-like features were observed growing from a primary Al_3Zr precipitate. Corner growth of precipitates has been observed for $L1_2$-Al_3Zr [43], and $L1_2$-Al_3Sc [44] growing from the liquid and $L1_2$-Ni_3Al [45] precipitates growing from solid solution within a Ni(Al) matrix. Preferential corner growth of cuboidal precipitates exists for Ni_3Al precipitates with positive misfits (larger lattice parameter for precipitate than matrix) in Ni-base superalloys [45]. In the case where there is a positive misfit, as is the case with Al_3Zr in an Al matrix, the compressive stresses on the precipitate are at a minimum in the <111> direction which therefore becomes the favorable growth direction [45]. The low strain also allows for a more favorable diffusion path resulting in further <111> growth [45]. Haugan et al. observed Al_3Zr precipitates with a dendritic appearance in an Al-1.4Zr (wt.%) alloy cooled at intermediate cooling rates (~200°C/s). Precipitates with a dendritic appearance have also been observed in our alloy (shown in Supplement Figures 1 and 2). Hyde et al. observed the same behavior for Al_3Sc precipitates in a Al-0.7Sc (wt.%) alloy cooled at 1000°C/s and attributed the corner growth due to the large constitutional undercooling gradients that are present at the cube corners compared to the cube faces. In the in-situ experiment shown in Figure 7, it is likely that the corner growth mechanism observed previously for Ni_3Al precipitates is active since the other mechanisms are operative during solidification rather than in the solid state. The horn-like features eventually disappeared at 450°C and this may be due to dissolution into the matrix and/or

re-precipitation to nearby coarsening precipitates. Interestingly, the grain boundary that was pinned earlier in the experiment (Figure 7(b)) by the dark particle still remains pinned even at a temperature of 500˚C (Figure 7(c)). This is direct evidence for impurity particles effectively pinning grain boundaries during elevated temperature exposure.

4.2 High-temperature mechanical behavior

The trend in room-temperature yield strengths (Figure 8) for the high-Zr alloy (Al-2.90Mg-2.10Zr, wt. %, Batch 3) is expected for a precipitation strengthened alloy: (i) aged, precipitated samples show higher yield strengths than the as-fabricated samples without precipitates. At test temperatures of 177˚C and above, the yield strengths of the aged, and overaged samples fall below that of the as-fabricated samples, dropping by a factor of three at 260˚C. The elevated temperature behavior is not as expected from an alloy that is precipitation-strengthened by thermally-stable ordered intermetallic phases with a uniform microstructure, as described below.

When considering this material's elevated temperature mechanical behavior it is important to recall that the bimodal grain microstructure consists of fine-grained regions with sub-micron equiaxed grains, and coarse-grain regions of columnar grains 1 to 5 μm in width and up to 40 μm in length. Despite the columnar grains being referred to as the coarse-grain region, the microstructure is still fine-grained compared to a conventionally-cast alloy. In a prior study, we reported an equiaxed grain size of 770±340 nm for a peak aged sample (8 h at 400˚C) and an equiaxed grain size of 1280±660 nm for an overaged sample (144 h at 400˚C) [15]. While grain coarsening occurs at elevated temperatures, the very modest growth suggests that grain boundary precipitates, such as Fe-rich intermetallics, Mg_2Si particles, grain-boundary Al_3Zr and especially Mg-rich oxides (as they do not change even at elevated temperatures as described above), are effective at impeding coarsening and maintaining the fine-grain size. Elevated temperature deformation of fine-grain aluminum alloys is often controlled by grain boundary sliding (GBS). Li et al. performed tensile tests between 450 and 570˚C on an Al-5038 alloy (Al-4.5Mg-0.18Fe-0.6Mn-0.1-Si-0.12Cr-0.02Ti wt.%) with a 20 μm grain size and found that the material had superplastic behavior, which was attributed to GBS, controlled by intergranular dislocation climb, and conventional dislocation creep [46]. While the temperature range tested by these authors is much higher than in the present study, the grain size in our material is ~20 times smaller (corresponding to ~8,000 time decrease in grain volume). Small grain sizes are well known to reduce the temperature required for superplastic behavior [47]. The high-temperature deformation in alloys with our observed grain sizes can likely be attributed to GBS, however, the grain boundary precipitates responsible for maintaining the fine grain size during elevated temperature will also serve to impede grain boundary sliding. The lower yield strength of the thermally treated samples over the as processed state is potentially due to the coarsening of grain boundary strengthening phases such as Fe-rich intermetallics and Mg_2Si particles. Tang et al. [48] tested the high-temperature properties of an ultrafine-grained Al-5083 alloy and an ultrafine-grained Al-5083 that had SiC reinforcement and found the reinforced alloy had superior high-temperature strength. They attributed this difference to the presence of grain-boundary

SiC particles that inhibited GBS [48]. A similar situation may be at play in our alloy but, instead of SiC on the grain boundaries, a combination of Fe-rich intermetallic, Mg_2Si particles, and grain boundary Al_3Zr inhibits GBS. While these grain boundary particles will occur in both the aged and as-fabricated alloy, the coarsening during thermal treatment, as shown in Figure 3, will reduce their effectiveness, explaining the greater yield strengths of the as-fabricated alloy.

The fine grain size of the tested alloy may mean that grain boundary diffusion is dominant, hence a stress exponent of 1-2 could be active. Sklenicka et al. [49] performed creep tests at 200 ºC on an ultrafine-grained (0.55 µm) Al-0.2Sc (wt.%) alloy produced by equal channel angular processing and in a second study [50] attributed this behavior to superplastic flow via GBS, which is generally associated with a stress exponent of $n = 2$. Marquis et al. [35] performed creep testing at 300˚C of an Al-2Mg-0.2Sc wt.% alloy, which is also solid-solution- and $L1_2$-precipitation strengthened, and attributed the creep behavior to dislocation glide creep with a stress exponent of $n = 3$. As can be seen in Figure 9, using n values of 1 leads to a poor fit, while $n = 2$ or 3 more accurately fit the experimental data for the tested samples; a better fit is achieved with $n = 3$, suggesting that dislocation glide is the limiting creep mechanism; however, GBS may still contribute to the overall strain as Rachinger GBS (grain boundary sliding without grain shape change that is accommodated by intragranular dislocation movement in adjacent grains) was found to have a stress exponent of 3, as this form of GBS is dislocation controlled [51]. The presence of the grain boundary precipitates likely inhibits GBS to some extent, forcing GBS to make up a smaller portion of the total creep strain, but the potential contribution from dislocation and Rachinger GBS was not calculated.

STEM analysis of the microstructure of the as-fabricated samples crept for 8 h and crept at 168 h revealed the presence of discontinuous precipitation (Figure 10). Since discontinuous precipitates were not present in the as-fabricated samples, the precipitation may occur during the creep test. The diffusivity of Zr in Al at the temperature of the creep test, 260˚C , is six orders of magnitude lower than the diffusivity at peak aging temperature, 400 ˚C (1.4 x10^{-25} vs. 1.6 x 10^{-19} m^2s^{-1}) suggesting that minimal to no Al_3Zr precipitation would usually be expected during 8 h at 260˚C; however, most theories describing the growth kinetics of discontinuous precipitation consider grain-boundary diffusion and not bulk diffusion [52]. Since grain boundary diffusion is several orders of magnitude faster than bulk diffusion [53], it is plausible that discontinuous precipitation can occur at 260˚C. It is also important to note that discontinuous precipitation reactions can be enhanced by the presence of strain [52], which is present in a creep test. Microstructural changes during creep testing of the as-fabricated samples suggest that the fitted stress exponent of 3 may not be representative of the actual creep limiting mechanisms.

Both as-fabricated and peak-aged alloys exhibit similar creep properties at 260˚C for the long duration test. The similarity of the creep behavior between the as fabricated and peak aged conditions for the long duration test may be due to aging that occurred in the as-fabricated sample during the 120 h of high-temperature exposure, before measurable deformation was

achieved at 15 MPa. The short duration creep tests (8 h) show substantially improved creep behavior for the as-fabricated samples with a threshold stress that is triple that measured in the long-duration creep test (41 vs. 13 MPa). A possible explanation for this behavior is grain-boundary particle coarsening occurring during the long duration creep test as clearly observed in Figure 10. Coarsening would result in less effective grain-boundary pinning, thus lowering threshold stresses for deformation. The annealed samples have reduced creep performance compared to the as-fabricated sample during the short duration creep test, which may also be explained by grain-boundary particle coarsening that occurs during the under-aging treatment. Again, isolating the exact creep limiting mechanisms is difficult due to the many microstructural changes occurring during creep testing.

5. Conclusions

The microstructural response to aging and creep deformation was investigated in two Al-Mg-Zr alloys (Al-3.6Mg-1.2Zr and Al-2.9Mg-2.1Zr, wt.%) processed by laser-based powder-bed additive manufacturing. It was concluded that:

- Both continuous and discontinuous precipitation of coherent, secondary $L1_2$-Al_3Zr occurs during peak aging (400˚C, 8 h). The continuous precipitates are spheroidal (~2 nm in diameter) and the discontinuous precipitates are highly elongated (~5 nm wide and hundreds of nanometers in length).

- The grain microstructure of the as-fabricated samples consists of fine-grained regions with sub-micron equiaxed grains, and coarse-grain regions of columnar grains 1 to 5 µm in width and up to 40 µm in length. Submicron precipitates - including Fe-rich particles, Mg_2Si particles, and Al_3Zr - are observed at the grain-boundaries of the alloys in the as-fabricated and peak-aged (400˚C, 8 h) conditions.

- The as-fabricated alloys display higher yield strengths than the peak-aged alloys at temperatures of 150˚C and above. At 260˚C, the as-fabricated and the peak-aged alloys (400˚C, 8 h) show widely different yield strengths of 87 and 24 MPa, respectively. This strength reduction in the aged condition is attributed to the coarsening of grain-boundary precipitates during aging, which leads to less inhibition of grain-boundary sliding.

- Creep data at 260 ºC can be well fitted with a stress exponents n=2 or 3 (indicative of GBS or dislocation motion) and a threshold stress (from precipitation strengthening).

- During long-duration (168 h) creep tests, both as-fabricated and peak-aged samples display nearly-identical creep behavior, with the same threshold stress of ~14 MPa. The similarity in creep properties is explained by the in-situ aging that occurs for the as-fabricated sample during the creep test at 260 ºC.

- For short-duration (8 h) creep tests, as-fabricated samples show a much higher threshold stress than samples previously aged at 260 ˚C for 168 h (~40 vs. ~14 MPa). This is again consistent with different exposure times at 260 ˚C (8 vs. 176 h), during which grain-boundary particles are coarsening.

6. References

[1] D. Thomas, S. Gilbert, Costs and Cost Effectiveness of Additive Manufacturing, (2014). https://doi.org/10.6028/NIST.SP.1176.

[2] J.H. Martin, B.D. Yahata, J.M. Hundley, J.A. Mayer, T.A. Schaedler, T.M. Pollock, 3D printing of high-strength aluminium alloys, Nature. 549 (2017) 365–369.

[3] L.N. Carter, C. Martin, P.J. Withers, M.M. Attallah, The influence of the laser scan strategy on grain structure and cracking behaviour in SLM powder-bed fabricated nickel superalloy, Journal of Alloys and Compounds. 615 (2014) 338–347. https://doi.org/10.1016/j.jallcom.2014.06.172.

[4] E.O. Olakanmi, Selective laser sintering/melting (SLS/SLM) of pure Al, Al–Mg, and Al–Si powders: Effect of processing conditions and powder properties, Journal of Materials Processing Technology. 213 (2013) 1387–1405. https://doi.org/10.1016/j.jmatprotec.2013.03.009.

[5] N.T. Aboulkhair, I. Maskery, C. Tuck, I. Ashcroft, N.M. Everitt, The microstructure and mechanical properties of selectively laser melted AlSi10Mg: The effect of a conventional T6-like heat treatment, Materials Science and Engineering: A. 667 (2016) 139–146. https://doi.org/10.1016/j.msea.2016.04.092.

[6] N.T. Aboulkhair, N.M. Everitt, I. Ashcroft, C. Tuck, Reducing porosity in AlSi10Mg parts processed by selective laser melting, Additive Manufacturing. 1 (2014) 77–86. https://doi.org/10.1016/j.addma.2014.08.001.

[7] E. Brandl, U. Heckenberger, V. Holzinger, D. Buchbinder, Additive manufactured AlSi10Mg samples using Selective Laser Melting (SLM): Microstructure, high cycle fatigue, and fracture behavior, Materials & Design. 34 (2012) 159–169. https://doi.org/10.1016/j.matdes.2011.07.067.

[8] N. Read, W. Wang, K. Essa, M.M. Attallah, Selective laser melting of AlSi10Mg alloy: Process optimisation and mechanical properties development, Materials & Design (1980-2015). 65 (2015) 417–424. https://doi.org/10.1016/j.matdes.2014.09.044.

[9] M.L. Montero-Sistiaga, R. Mertens, B. Vrancken, X. Wang, B. Van Hooreweder, J.-P. Kruth, J. Van Humbeeck, Changing the alloy composition of Al7075 for better processability by selective laser melting, Journal of Materials Processing Technology. 238 (2016) 437–445. https://doi.org/10.1016/j.jmatprotec.2016.08.003.

[10] Q. Jia, P. Rometsch, P. Kürnsteiner, Q. Chao, A. Huang, M. Weyland, L. Bourgeois, X. Wu, Selective laser melting of a high strength AlMnSc alloy: Alloy design and strengthening mechanisms, Acta Materialia. 171 (2019) 108–118. https://doi.org/10.1016/j.actamat.2019.04.014.

[11] R. Li, M. Wang, T. Yuan, B. Song, C. Chen, K. Zhou, P. Cao, Selective laser melting of a novel Sc and Zr modified Al-6.2Mg alloy: Processing, microstructure, and properties, Powder Technology. 319 (2017) 117–128. https://doi.org/10.1016/j.powtec.2017.06.050.

[12] A.B. Spierings, K. Dawson, P. Dumitraschkewitz, S. Pogatscher, K. Wegener, Microstructure characterization of SLM-processed Al-Mg-Sc-Zr alloy in the heat treated and HIPed condition, Additive Manufacturing. 20 (2018) 173–181. https://doi.org/10.1016/j.addma.2017.12.011.

[13] L. Zhou, H. Pan, H. Hyer, S. Park, Y. Bai, B. McWilliams, K. Cho, Y. Sohn, Microstructure and tensile property of a novel AlZnMgScZr alloy additively manufactured by gas atomization and laser powder bed fusion, Scripta Materialia. 158 (2019) 24–28. https://doi.org/10.1016/j.scriptamat.2018.08.025.

[14] A.B. Spierings, K. Dawson, T. Heeling, P.J. Uggowitzer, R. Schäublin, F. Palm, K. Wegener, Microstructural features of Sc- and Zr-modified Al-Mg alloys processed by selective laser melting, Materials & Design. 115 (2017) 52–63. https://doi.org/10.1016/j.matdes.2016.11.040.

[15] J.R. Croteau, S. Griffiths, M.D. Rossell, C. Leinenbach, C. Kenel, V. Jansen, D.N. Seidman, D.C. Dunand, N.Q. Vo, Microstructure and mechanical properties of Al-Mg-Zr alloys processed by selective laser melting, Acta Materialia. 153 (2018) 35–44. https://doi.org/10.1016/j.actamat.2018.04.053.

[16] K. Schmidtke, F. Palm, A. Hawkins, C. Emmelmann, Process and Mechanical Properties: Applicability of a Scandium modified Al-alloy for Laser Additive Manufacturing, Physics Procedia. 12 (2011) 369–374. https://doi.org/10.1016/j.phpro.2011.03.047.

[17] A.B. Spierings, K. Dawson, M. Voegtlin, F. Palm, P.J. Uggowitzer, Microstructure and mechanical properties of as-processed scandium-modified aluminium using selective laser melting, CIRP Annals - Manufacturing Technology. 65 (2016) 213–216. https://doi.org/10.1016/j.cirp.2016.04.057.

[18] K.E. Knipling, D.C. Dunand, D.N. Seidman, Criteria for developing castable, creep-resistant aluminum-based alloys - A review, International Journal of Materials Research. 97 (2006) 246–265.

[19] A.B. Spierings, K. Dawson, K. Kern, F. Palm, K. Wegener, SLM-processed Sc- and Zr-modified Al-Mg alloy: Mechanical properties and microstructural effects of heat treatment, Materials Science and Engineering: A. 701 (2017) 264–273. https://doi.org/10.1016/j.msea.2017.06.089.

[20] J.A. Lyndon, R.K. Gupta, M.A. Gibson, N. Birbilis, Electrochemical behaviour of the β-phase intermetallic (Mg2Al3) as a function of pH as relevant to corrosion of aluminium–magnesium alloys, Corrosion Science. 70 (2013) 290–293. https://doi.org/10.1016/j.corsci.2012.12.022.

[21] I.G. Brodova, I.V. Polents, D.V. Bashlikov, P.S. Popel, O.A. Chikova, The forming mechanism of ultradispersed phases in rapidly solidified aluminium alloys, Nanostructured Materials. 6 (1995) 477–479. https://doi.org/10.1016/0965-9773(95)00100-X.

[22] A. De Luca, D.C. Dunand, D.N. Seidman, Mechanical properties and optimization of the aging of a dilute Al-Sc-Er-Zr-Si alloy with a high Zr/Sc ratio, Acta Materialia. 119 (2016) 35–42. https://doi.org/10.1016/j.actamat.2016.08.018.

[23] A. De Luca, D.C. Dunand, D.N. Seidman, Microstructure and mechanical properties of a precipitation-strengthened Al-Zr-Sc-Er-Si alloy with a very small Sc content, Acta Materialia. 144 (2018) 80–91. https://doi.org/10.1016/j.actamat.2017.10.040.

[24] S.P. Wen, K.Y. Gao, H. Huang, W. Wang, Z.R. Nie, Precipitation evolution in Al–Er–Zr alloys during aging at elevated temperature, Journal of Alloys and Compounds. 574 (2013) 92–97. https://doi.org/10.1016/j.jallcom.2013.03.237.

[25] S. Griffiths, M.D. Rossell, J. Croteau, N.Q. Vo, D.C. Dunand, C. Leinenbach, Effect of laser rescanning on the grain microstructure of a selective laser melted Al-Mg-Zr alloy, Materials Characterization. 143 (2018) 34–42. https://doi.org/10.1016/j.matchar.2018.03.033.

[26] K.E. Knipling, D.C. Dunand, Creep resistance of cast and aged Al–0.1Zr and Al–0.1Zr–0.1Ti (at.%) alloys at 300–400°C, Scripta Materialia. 59 (2008) 387–390. https://doi.org/10.1016/j.scriptamat.2008.02.059.

[27] K.E. Knipling, The Effect of Group 5 (V, Nb, Ta) Additions on Precipitation in Al-Sc Alloys, Microscopy and Microanalysis. 22 (2016) 688–689. https://doi.org/10.1017/S1431927616004293.

[28] D. Erdeniz, W. Nasim, J. Malik, A.R. Yost, S. Park, A. De Luca, N.Q. Vo, I. Karaman, B. Mansoor, D.N. Seidman, D.C. Dunand, Effect of vanadium micro-alloying on the microstructural evolution and creep behavior of Al-Er-Sc-Zr-Si alloys, Acta Materialia. 124 (2017) 501–512. https://doi.org/10.1016/j.actamat.2016.11.033.

[29] D. Erdeniz, A. De Luca, D.N. Seidman, D.C. Dunand, Effects of Nb and Ta additions on the strength and coarsening resistance of precipitation-strengthened Al-Zr-Sc-Er-Si alloys, Materials Characterization. 141 (2018) 260–266. https://doi.org/10.1016/j.matchar.2018.04.051.

[30] Z.-H. Jia, H.-L. Huang, X.-L. Wang, Y. Xing, Q. Liu, Hafnium in Aluminum Alloys: A Review, Acta Metallurgica Sinica (English Letters). 29 (2016) 105–119. https://doi.org/10.1007/s40195-016-0379-0.

[31] A. De Luca, D.N. Seidman, D.C. Dunand, Effects of Mo and Mn microadditions on strengthening and over-aging resistance of nanoprecipitation-strengthened Al-Zr-Sc-Er-Si alloys, Acta Materialia. 165 (2019) 1–14. https://doi.org/10.1016/j.actamat.2018.11.031.

[32] R.A. Karnesky, D.N. Seidman, D.C. Dunand, Creep of Al-Sc Microalloys with Rare-Earth Element Additions, Materials Science Forum. 519–521 (2006) 1035–1040. https://doi.org/10.4028/www.scientific.net/MSF.519-521.1035.

[33] C. Booth-Morrison, D.N. Seidman, D.C. Dunand, Effect of Er additions on ambient and high-temperature strength of precipitation-strengthened Al–Zr–Sc–Si alloys, Acta Materialia. 60 (2012) 3643–3654. https://doi.org/10.1016/j.actamat.2012.02.030.

[34] M.E. Krug, D.N. Seidman, D.C. Dunand, Creep properties and precipitate evolution in Al–Li alloys microalloyed with Sc and Yb, Materials Science and Engineering: A. 550 (2012) 300–311. https://doi.org/10.1016/j.msea.2012.04.075.

[35] E.A. Marquis, D.N. Seidman, D.C. Dunand, Effect of Mg addition on the creep and yield behavior of an Al–Sc alloy, Acta Materialia. 51 (2003) 4751–4760. https://doi.org/10.1016/S1359-6454(03)00288-X.

[36] K.E. Knipling, D.C. Dunand, Creep resistance of cast and aged Al–0.1Zr and Al–0.1Zr–0.1Ti (at.%) alloys at 300–400°C, Scripta Materialia. 59 (2008) 387–390. https://doi.org/10.1016/j.scriptamat.2008.02.059.

[37] N.E. Uzan, R. Shneck, O. Yeheskel, N. Frage, High-temperature mechanical properties of AlSi10Mg specimens fabricated by additive manufacturing using selective laser melting technologies (AM-SLM), Additive Manufacturing. 24 (2018) 257–263. https://doi.org/10.1016/j.addma.2018.09.033.

[38] K.E. Knipling, D.C. Dunand, D.N. Seidman, Nucleation and Precipitation Strengthening in Dilute Al-Ti and Al-Zr Alloys, Metallurgical and Materials Transactions A. 38 (2007) 2552–2563. https://doi.org/10.1007/s11661-007-9283-6.

[39] A.V. Mikhaylovskaya, A.G. Mochugovskiy, V.S. Levchenko, N.Yu. Tabachkova, W. Mufalo, V.K. Portnoy, Precipitation behavior of L12 Al3Zr phase in Al-Mg-Zr alloy, Materials Characterization. 139 (2018) 30–37. https://doi.org/10.1016/j.matchar.2018.02.030.

[40] E. Nes, H. Billdal, The mechanism of discontinuous precipitation of the metastable Al3Zr phase from an Al-Zr solid solution, Acta Metallurgica. 25 (1977) 1039–1046. https://doi.org/10.1016/0001-6160(77)90133-X.

[41] N. Ryum, Precipitation and recrystallization in an A1-0.5 WT.% Zr-alloy, Acta Metallurgica. 17 (1969) 269–278. https://doi.org/10.1016/0001-6160(69)90067-4.

[42] Malgorzata Warmuzek, Intermetallic Phases in Aluminum-Silicon Technical Cast Alloys, in: Aluminum-Silicon Casting Alloys, ASM International, 2017.

[43] T. Haugan, E. Nes, N. Ryum, Precipitation Reactions in Ai-Zr-Alloys, MRS Proceedings. 21 (1982) 495. https://doi.org/10.1557/PROC-21-495.

[44] K.B. Hyde, A.F. Norman, P.B. Prangnell, The effect of cooling rate on the morphology of primary Al3Sc intermetallic particles in Al–Sc alloys, Acta Materialia. 49 (2001) 1327–1337. https://doi.org/10.1016/S1359-6454(01)00050-7.

[45] R.A. Ricks, A.J. Porter, R.C. Ecob, The growth of γ′ precipitates in nickel-base superalloys, Acta Metallurgica. 31 (1983) 43–53. https://doi.org/10.1016/0001-6160(83)90062-7.

[46] F. Li, Microstructural evolution and mechanismsof superplasticity in an Al-4-5%Mg alloy, Materials Science and Technology. 13 (1997) 17–23. https://doi.org/10.1179/mst.1997.13.1.17.

[47] S.B. Prabu, K.A. Padmanabhan, Chapter 8 - Superplasticity in and Superplastic Forming of Aluminum–Lithium Alloys, in: N. Eswara Prasad, A.A. Gokhale, R.J.H. Wanhill (Eds.), Aluminum-Lithium Alloys, Butterworth-Heinemann, Boston, 2014: pp. 221–258. https://doi.org/10.1016/B978-0-12-401698-9.00008-2.

[48] F. Tang, B.Q. Han, M. Hagiwara, J.M. Schoenung, Tensile Properties of a Nanostructured Al-5083/SiCp Composite at Elevated Temperatures, Advanced Engineering Materials. 9 (2007) 286–291. https://doi.org/10.1002/adem.200600270.

[49] V. Sklenicka, J. Dvorak, P. Kral, M. Svoboda, M. Kvapilova, T.G. Langdon, Factors influencing creep flow and ductility in ultrafine-grained metals, Materials Science and Engineering: A. 558 (2012) 403–411. https://doi.org/10.1016/j.msea.2012.08.019.

[50] M. Kawasaki, V. Sklenička, T.G. Langdon, An evaluation of creep behavior in ultrafine-grained aluminum alloys processed by ECAP, Journal of Materials Science. 45 (2010) 271–274. https://doi.org/10.1007/s10853-009-3975-9.

[51] T.G. Langdon, Grain boundary sliding revisited: Developments in sliding over four decades, Journal of Materials Science. 41 (2006) 597–609. https://doi.org/10.1007/s10853-006-6476-0.

[52] D. Williams, E. P. Butler, Grain Boundary Discontinuous Precipitation Reactions, 1981. https://doi.org/10.1179/imr.1981.26.1.153.

[53] C. Herzig, Y. Mishin, Grain Boundary Diffusion in Metals, in: P. Heitjans, J. Kärger (Eds.), Diffusion in Condensed Matter: Methods, Materials, Models, Springer Berlin Heidelberg, Berlin, Heidelberg, 2005: pp. 337–366. https://doi.org/10.1007/3-540-30970-5_8.